Chinese Journal of Chemical Engineering 88 (2025) 256–264

Contents lists available at ScienceDirect

Chinese Journal of Chemical Engineering

journal homepage: www.elsevier.com/locate/CJChE

Full Length Article

Copper hexacyanoferrate framework with dual redox centers for selective lithium extraction in hybrid capacitive deionization

Li Zhang [1, #], Shuyu Wang [1, #], Cuijiao Zhao [1, *], Menglong Liu [1], Tao Ye [2], Wenwen Ding [3, *], Hongjian Zhou [4, *], Zhongti Sun [2, 5, *], Weiji Dai [1], Saifang Huang [1, *]

[1] School of Materials Science and Engineering, Jiangsu University of Science and Technology, Zhenjiang 212100, China
[2] School of Materials Science and Engineering, Jiangsu University, Zhenjiang 212013, China
[3] School of Architecture and Civil Engineering, Jiangsu University of Science and Technology, Zhenjiang 212100, China
[4] Key Laboratory of Materials Physics, Anhui Key Laboratory of Nanomaterials and Nanotechnology, Institute of Solid State Physics, Hefei Institutes of Physical Science, Chinese Academy of Sciences, Hefei 230031, China
[5] School of Materials Science and Engineering, Anhui Province Key Laboratory of Efficient Conversion and Solid-State Storage of Hydrogen & Electricity, Anhui University of Technology, Maanshan 243002, China

ARTICLE INFO

Article history:
Received 27 July 2025
Received in revised form
3 September 2025
Accepted 4 September 2025
Available online 27 September 2025

Keywords:
Copper hexacyanoferrate
Desalination
Lithium extraction
Selective electrosorption
Recovery
Nanoparticles

ABSTRACT

Developing selective electrodes for lithium extraction from brines remains challenging. This work reports room-temperature synthesized cubic copper hexacyanoferrate (CuHCF) nanoparticles for hybrid capacitive deionization (HCDI). The CuHCF framework exhibits a high surface area (715.84 $m^2 \cdot g^{-1}$), dual redox-active sites ($[Fe^{III}(CN)_6]^{4-}/[Fe^{II}(CN)_6]^{3-}$ and Cu^{+}/Cu^{2+}), and excellent cyclability (99.4% capacity retention after 1000 cycles). In HCDI system, the CuHCF cathode demonstrates remarkable Li^+ ions selectivity, achieving a 25.5 $mg \cdot g^{-1}$ adsorption capacity in 500 $mg \cdot L^{-1}$ LiCl solution with 94% charge efficiency at 1.2 V. Notably, in mixed Li^+/Mg^{2+} solutions (30:1 molar ratio), CuHCF nanoparticles maintain a high separation coefficient of 3.1, attributed to the synergistic effects of ionic sieving and preferential redox interactions. Mechanistic studies confirm Li^+ (de)intercalation *via* reversible $[Fe^{III}(CN)_6]^{4-}/[Fe^{II}(CN)_6]^{3-}$ and Cu^{2+}/Cu^{+} transitions. Density functional theory calculations reveal Li^+ exhibits lower adsorption energy than Mg^{2+} (−3.72 eV *vs.* −1.49 eV), which fundamentally explains the preferential extraction capability of Li^+ ions over Mg^{2+} ions during the separation process. This study advances ion-selective pseudocapacitor design for sustainable lithium extraction from high-salinity resources.

1. Introduction

With the explosive growth of electronic products such as electric vehicles, laptops, and mobiles, along with the rise of energy storage devices, the market demand for lithium-ion batteries has surged, leading to a dramatic increase in global lithium prices over the past five years [1,2]. The development of lithium resources has become increasingly important. Lithium is primarily found in ores, salt lake brines, and seawater [3,4]. Notably, the lithium content in salt lake brines accounts for two-thirds of the total, and the cost of lithium extraction from salt lakes is only one-third that of extraction from ores [5,6]. Therefore, extracting lithium from salt lake brines and seawater offers significant advantages in terms of resource scale and cost-effectiveness, positioning it as a major trend in future lithium production [7–9]. In these salt lake brines, lithium-ion concentrations consistently exceed 150 $mg \cdot L^{-1}$, coexisting with substantial concentrations of alkali metal ions including potassium, sodium, calcium, and magnesium. Notably, Li^+ and Mg^{2+} exhibit analogous chemical properties, leading to their co-extraction during conventional evaporation, physical adsorption, and solvent extraction processes. This indiscriminate capture necessitates additional post-treatment procedures to achieve phase separation, thereby escalating operational costs and energy consumption. Consequently, the development of green lithium extraction technologies characterized by energy efficiency, environmental compatibility, low-temperature/pressure operation, and high-

* Corresponding authors.
E-mail addresses: 202100000134@just.edu.cn (C. Zhao), 202100000129@just.edu.cn (W. Ding), hjzhou@issp.ac.cn (H. Zhou), ztsun@ujs.edu.cn (Z. Sun), s.huang@just.edu.cn (S. Huang).
# These authors contributed equally in this work.

https://doi.org/10.1016/j.cjche.2025.09.008

efficiency Mg^{2+}/Li^{+} separation has emerged as a critical research frontier in sustainable resource recovery.

Capacitive deionization (CDI), as an emerging electrochemical lithium extraction technology, has garnered attention due to its advantages of high adsorption capacity, rapid adsorption/desorption rates, ease of regeneration, and environmental friendliness. By rationally designing electrode materials, corresponding CDI systems can achieve reversible and efficient adsorption of target ions, demonstrating high adsorption capacity and excellent selectivity [10,11]. Among these, hybrid capacitive deionization (HCDI) has been extensively reported for its high ion selectivity and removal capacity. This technology has been applied to the selective extraction of Li^{+} ions from salt lake brines [12–16]. HCDI typically consists of a pseudocapacitive battery material as the cathode and carbon-based materials as the anode [17,18]. Upon the application of an electric field, cations in the brine are captured in the cathode through Faradaic redox reactions, while anions are stored in the carbon anode by forming an electrical double layer [19,20]. By applying a reverse voltage or short-circuiting, both the cathode and anode materials can be easily regenerated in situ without the need for any chemical reagents, such as acids or bases [21,22]. Due to their high selectivity, material stability, and environmental friendliness, various HCDI systems have successfully used lithium manganese oxide ($LiMn_2O_4$, LMO) [12,23], lithium nickel manganese oxide ($LiNi_{0.5}Mn_{1.5}O_4$) [24], and lithium nickel cobalt manganese oxide ($Li(Ni_xCo_yMn_z)O_2$) [25] as active electrode materials for lithium extraction from salt lake brines [26]. However, these electrode materials, while selective for Li^{+} ions, have complex synthesis processes and low yields, making them inadequate to meet industrial demands. Therefore, the development of novel pseudocapacitive materials with enhanced charge adsorption capacity and selective extraction of Li^{+} ions remains essential.

Prussian blue analogues (PBAs) are common cation intercalation materials characterized by a three-dimensional open framework structure. Their unique crystal structure and abundant ionic channels facilitate the rapid transport and storage of cations, providing a foundation for cation (de)intercalation. Specifically, PBAs are typically represented by the chemical formula $A_xM'[M(CN)_6]_y \cdot nH_2O$ ($0 \le x \le 2$, $0 \le y \le 1$), where A denotes an alkali metal ion, and M/M′ represents transition metal ions. This structure, abbreviated as M'HCF, features alternating M and M′ atoms connected by cyanide ligands (M−C≡N−M′), forming a face-centered cubic lattice. Within this crystal structure, there are channels or interlayer spaces of specific sizes and charge environments that only allow cations with particular ionic radii and charge characteristics to enter and be adsorbed effectively [27]. Among them, cubic copper hexacyanoferrate (CuHCF) exhibits two sets of redox couples ($[Fe^{III}(CN)_6]^{4-}/[Fe^{II}(CN)_6]^{3-}$ and Cu^{2+}/Cu^{+}), with relatively low redox potentials that favor the stable electrochemical performance of CuHCF electrode materials in saline solutions. More importantly, these two redox reactions significantly enhance the specific capacitance of CuHCF electrode, thereby facilitating the capture of more Li^{+} ions during lithium extraction. Additionally, the $[Fe^{III}(CN)_6]^{4-}/[Fe^{II}(CN)_6]^{3-}$ and Cu^{2+}/Cu^{+} redox pairs exhibit high stability and reversibility, providing excellent cycling stability for the CuHCF electrode. Consequently, CuHCF is promising as a novel pseudocapacitive electrode material with a high capacitance adsorption capacity and exceptional selectivity for Li^{+} ions.

Herein, we introduce a facile room-temperature co-precipitation method to synthesize CuHCF nanoparticles for efficient lithium-selective extraction *via* HCDI system. The composition, structure, and physicochemical properties of the synthesized CuHCF nanoparticles were systematically characterized. The CuHCF sample was utilized as the cathode, coupled with an aminated activated carbon (A-AC) anode, to assemble a membrane-free HCDI system. Batch experiments were conducted to assess the lithium extraction performance and cycling stability of CuHCF nanoparticles. Additionally, XPS analysis, electrochemical measurements and density functional theory (DFT) calculations were employed to elucidate the mechanism underlying the selective lithium extraction of CuHCF electrode. The experimental results underscore the potential of CuHCF for lithium extraction in HCDI system.

2. Experimental

2.1. Preparation of CuHCF nanoparticles

A 0.1 $mol \cdot L^{-1}$ solution of copper(II) nitrate trihydrate ($Cu(NO_3)_2 \cdot 3H_2O$) was prepared by dissolving it in 50 ml of deionized water, forming solution A. Concurrently, another clear solution B was prepared by adding 0.05 $mol \cdot L^{-1}$ potassium ferricyanide ($K_3Fe(CN)_6$) to 50 ml of deionized water. Subsequently, both solutions were simultaneously added dropwise through a constant drop funnel into 25 ml of vigorously stirred deionized water. The mixture was stirred at room temperature for 30 min, followed by a standing period of 32 h. After the reaction was completed, the resulting precipitate was collected by centrifugation and washed with deionized water to remove excess impurities. Finally, the sample was dried in an oven at 60 °C to obtain the CuHCF nanoparticles. The information of starting materials and characterization methods are given in the Supplementary Material.

2.2. HCDI measurements

The desalination experiment in the HCDI system utilizes a LiCl solution for continuous cycling tests. The HCDI testing setup comprises a peristaltic pump, a conductivity meter, a DC power supply, a homemade HCDI unit, and a reservoir. The size of the HCDI electrodes are 40 mm × 40 mm. A mixture consisting of 80% (mass) active material, 10% (mass) carbon black, and 10% (mass) PVDF is prepared in *N*-methylpyrrolidone (NMP) to form a homogeneous slurry. The slurry was uniformly coated onto carbon paper and placed in an oven at 60 °C to dry 12 h. The total mass of the active sample for the HCDI tests was 100 mg. During the testing process, the prepared active sample served as the cathode material of the HCDI, while A-AC was utilized as the anode material. Carbon paper acted as the current collector, and a 1.0 mm thick silicone sheet functioned as the separator between the cathode and anode. A LiCl solution with a concentration of 500 $mg \cdot L^{-1}$ was continuously pumped into the HCDI unit *via* a peristaltic pump at a flow rate of 8 $ml \cdot min^{-1}$. The lithium extraction voltage was set at 1.2 V, and changes in the conductivity of the LiCl solution were monitored using a conductivity meter (DDSJ-307F, Leici, China). During the Li^{+} ions (de)intercalation process, the conductivity of the LiCl solution was recorded every 20 s. The salt adsorption capacity (SAC, $mg \cdot g^{-1}$) was calculated using the following formula:

$$SAC = (C_0 - C_t)V/m \quad (1)$$

where C_0 and C_t denote the initial and any time t concentrations of the LiCl solution, respectively. V refers to the volume of the LiCl solution, and m represents the total mass of the active material in both electrodes.

The average adsorption rate (SAR, $mg \cdot g^{-1} \cdot min^{-1}$) of the HCDI electrode materials is calculated according to the following equation:

$$SAR = SAC/t \quad (2)$$

where t (s) denotes the lithium extraction time.

The charge efficiency (CE) of the HCDI electrode materials is calculated using the following formula:

$$CE = \frac{FV(C_0 - C_t)}{M\int Idt} \quad (3)$$

where F is Faraday's constant (96485 $C \cdot mol^{-1}$), V is the volume of the LiCl solution, C_0 and C_t represent the initial concentration and the concentration at any time t of the LiCl solution, respectively. M indicates the average molar mass of the cations and anions in the LiCl solution (with LiCl having a molar mass of 42.39 $g \cdot mol^{-1}$), and I is the applied current, while t represents the duration of the lithium extraction process.

The concentration of metal ions was measured using an inductively coupled plasma optical emission spectrometer (ICP). To evaluate the selective lithium extraction performance of CuHCF electrode, the selectivity separation coefficient of Li^+ ions relative to other impurity ions was calculated using the following formula:

$$\alpha_{Li/X} = \frac{Q_{Li^+}/M_{Li^+}}{Q_X/M_X} \times \frac{C_{0,X}}{C_{0,Li^+}} \quad (4)$$

Q_{Li^+} and Q_X represent the respective electroadsorption amounts of Li^+ and impurity ions (*e.g.*, Mg^{2+}); M_{Li^+} and M_X denote the relative atomic masses of Li^+ and the impurity ions (Mg^{2+}), respectively; and C_{0,Li^+} and $C_{0,X}$ indicate the initial concentrations of Li^+ ions and the impurity ions (Mg^{2+}) in the solution.

3. Results and Discussion

3.1. Material characterization

The synthesis process of CuHCF nanoparticles is illustrated in Fig. S1. To determine the structural and morphological characteristics of CuHCF nanoparticles, multiple structural characterization techniques were employed. As shown in Fig. 1(a), the CuHCF nanoparticles synthesized *via* chemical co-precipitation matches well with the standard XRD pattern (JCPDS card NO. 86-0513). The characteristic peaks correspond to the (111), (200), (220), (400), and (420) crystal planes, and no impurity peaks are observed, confirming the absence of any phases other than CuHCF. The CuHCF crystallizes in a cubic system with the space group $Fm\bar{3}$ m, where octahedrally coordinated Cu and Fe are bridged by C≡N. The C≡N bonds construct a semi-filled body-centered channel for ion transport, forming a three-dimensional open framework structure, which provides an ideal pathway for the reversible (de)intercalation of Li^+ ions. The SEM and TEM images of CuHCF nanoparticles are shown in Fig. 1(b) and (c), respectively. The CuHCF nanoparticles exhibit a primary particle size of approximately 200 nm. TEM images further confirm that CuHCF consists of nanocubic particles around 200 nm in size. EDS mapping reveals that the CuHCF nanoparticles are composed of Cu, Fe, C, and N, demonstrating their homogeneous elemental distribution (Fig. 1(d)).

The coordination environment of the CuHCF chemical bonds was elucidated using FT-IR and Raman spectroscopy. As shown in Fig. S2(a), an absorption peak at 2103 cm^{-1} was detected, attributable to the stretching vibration of the C≡N group. The absorption peaks at 592 and 667 cm^{-1} were assigned to the vibrations of Fe–CN–Cu. Additionally, another peak was observed at approximately 3428 cm^{-1}, corresponding to the O–H stretching vibration. The Raman spectrum of the CuHCF nanoparticles exhibits a strong vibrational band at 2149 cm^{-1}, primarily attributed to the stretching vibration of the C≡N bond in the cyanide groups within the copper hexacyanoferrate (Fig. S2(b)). Collectively, the results from FT-IR and Raman spectroscopy provide compelling evidence for the successful synthesis of CuHCF nanoparticles.

Pore size plays a pivotal role in ion diffusion kinetics, which significantly influences the performance of HCDI systems. The porosity and pore size distribution of the CuHCF nanoparticles were determined *via* BET test. As illustrated in Fig. S2(c), the CuHCF sample exhibits a Type-IV isotherm, characterized by a distinct hysteresis loop in the range of 0.4–1.0, indicative of mesoporous structures within the CuHCF nanoparticles. These mesopores can offer additional migration pathways for Li^+ ions. The pore size distribution curve reveals a narrow pore structure within the CuHCF sample. The average pore size of the CuHCF sample is approximately 4 nm, suggesting the presence of abundant microporous and mesoporous structures (Fig. S2(d)). The specific surface area of the CuHCF nanoparticles was measured to be 715.84 $m^2 \cdot g^{-1}$. This high specific surface area and the abundant pore structure of CuHCF nanoparticles can provide more adsorption and reaction sites for Li^+ ion adsorption, thus enhancing lithium extraction performance.

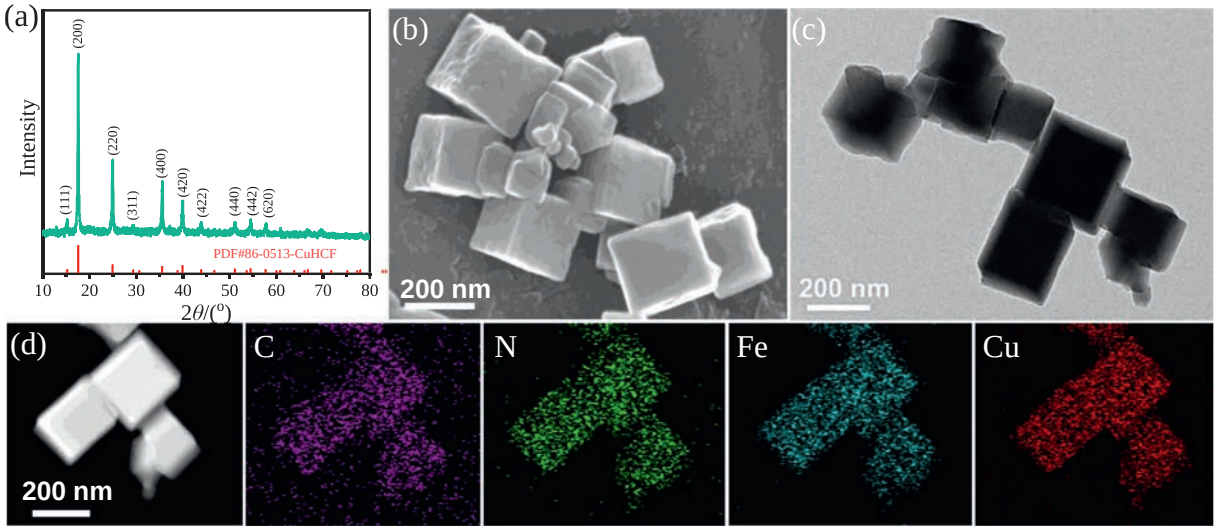

Fig. 1. (a) XRD pattern of CuHCF nanoparticles; (b)–(c) SEM and TEM images of CuHCF nanoparticles; (d) elemental mappings of CuHCF nanoparticles with C, N, Fe, and Cu.

XPS analysis was employed to determine the chemical composition and electronic states of the elements within the CuHCF sample. The survey spectrum of the CuHCF sample revealed the presence of C, Fe, N, and Cu elements, with no detectable impurities (Fig. S3). As shown in Fig. S4(a), the high-resolution Fe 2p spectrum exhibited characteristic peaks at binding energies of 708.3 and 721.3 eV, corresponding to Fe $2p_{3/2}$ and Fe $2p_{1/2}$ of Fe^{2+}, respectively, while peaks located at 709.9 and 723.5 eV were assigned to Fe $2p_{3/2}$ and Fe $2p_{1/2}$ of Fe^{3+}, respectively. Furthermore, satellite peaks were observed at 711.4 and 724.8 eV, corresponding to Fe $2p_{3/2}$ and Fe $2p_{1/2}$, respectively [28]. In addition, the high-resolution Cu 2p spectrum was fitted with four characteristic peaks: peaks at 933.0 and 952.6 eV corresponding to Cu $2p_{3/2}$ and Cu $2p_{1/2}$ of Cu^{+}, respectively, and peaks at 935.3 and 955.4 eV corresponding to Cu $2p_{3/2}$ and Cu $2p_{1/2}$ of Cu^{2+}, respectively. Satellite peaks were also observed at 943.9 and 963.3 eV, corresponding to Cu $2p_{3/2}$ and Cu $2p_{1/2}$, respectively (Fig. S4(b)) [29]. As shown in Fig. S4(c), the high-resolution C 1s spectrum exhibited characteristic peaks at 284.7, 285.5, 286.1, and 288.5 eV, corresponding to C—C/C═C, C≡N, C—O, and O—C═O, respectively [30]. Concurrently, deconvoluted peaks in the high-resolution N 1s spectrum at 398.3, 399.3, and 402.4 eV all indicated the presence of C≡N groups within the CuHCF nanoparticles (Fig. S4(d)) [30]. These results collectively confirm the successful synthesis of CuHCF nanoparticles.

3.2. Electrochemical capacitance performance

To evaluate the electrochemical extraction characteristics of CuHCF electrode for Li^{+} ions, a systematic investigation was conducted using a three-electrode system comprising a working electrode, a counter electrode (Pt mesh), and a reference electrode (Ag/AgCl) in a 1.0 $mol \cdot L^{-1}$ LiCl electrolyte. As illustrated in Fig. S5 (a), the redox peaks observed at 0.28 V and 0.39 V are likely attributed to the Fe^{2+}/Fe^{3+} redox couple. Specifically, the reduction peak at 0.28 V can be ascribed to the insertion of Li^{+} ions, while the oxidation peak at 0.39 V corresponds to the extraction of Li^{+} ions. The presence of this redox pair indicates that Fe serves as a crucial electrochemical active site within the CuHCF crystal framework, facilitating the reversible participation in the (de) intercalation reactions of Li^{+} ions. This reversibility is derived from the unique open-framework structure of CuHCF, which possesses voids that allow for rapid Li^{+} ions migration during charge and discharge processes. Concurrently, another pair of redox peaks observed at 0.58 V and 0.62 V can be assigned to the Cu^{+}/Cu^{2+} redox reactions. The cathodic peak at 0.58 V is associated with the insertion of Li^{+} ions, whereas the anodic peak at 0.62 V is related to the extraction of Li^{+} ions. Acting as another active site in the CuHCF structure, Cu also participates in the storage and release processes of Li^{+} ions. The Cu^{+}/Cu^{2+} redox reactions further enhance the capacitive performance of the CuHCF electrode, enabling it to store a greater number of Li^{+} ions. Additionally, the peak positions exhibit slight shifts with varying scan rates, which can be attributed to concentration polarization at higher scan rates [31]. Nevertheless, despite the increase in scan rate from 1 to 20 $mV \cdot s^{-1}$, the oxidation and reduction peaks remain evident in the CV curves, and the overall shape of the CV profiles remains consistent, indicating that the CuHCF electrode exhibits stable electrochemical behavior and high Faradaic activity. Fig. S5(b) presents the galvanostatic charge-discharge (GCD) curves of the CuHCF electrode in 1.0 $mol \cdot L^{-1}$ LiCl solution at different current densities. During GCD testing, the discharge behavior is considered a critical indicator of the electrosorption performance. At various current densities, the GCD curves of the CuHCF electrode display asymmetric quasi-triangular shapes, suggesting that the Li^{+} ions electrosorption behavior originates from Faradaic redox reactions.

To elucidate the pseudocapacitive behavior of Li^{+} ions in CuHCF electrodes, the charge storage mechanism was systematically analyzed based on Dunn's classical theoretical framework [32]. According to this theory, the charge storage process in electrodes can be categorized into two distinct modes: diffusion-controlled and surface capacitive-controlled mechanisms. The relationship between the measured current (i) and scan rate (v) was quantitatively described using Eq. (S2). The capacitive contributions at each scan rate were calculated *via* Eq. (S3), where k_1v represents the contribution from surface capacitive-controlled processes and $k_2v^{1/2}$ corresponds to diffusion-controlled processes [33]. Through quantitative analysis of the correlation between current and scan rate, coupled with the deconvolution of individual curves at constant potentials, it was revealed that the surface capacitive-controlled processes account for 95% of the total capacity at a scan rate of 20 $mV \cdot s^{-1}$ (Fig. 2(a)). This finding underscores the dominant influence of surface capacitive behavior in the electrochemical processes of Li^{+} ions within CuHCF electrode. Notably, b value of 0.5 signifies diffusion-controlled behavior, while b value of 1.0 indicates ideal capacitive-controlled behavior [33]. By fitting the logarithmic plots of response current versus scan rate at oxidation and reduction potentials, the calculated b values at oxidation potentials were 0.95 and 0.96, whereas those at reduction potentials were 0.98 and 0.87. These results conclusively confirm the near-ideal capacitive-controlled behavior of CuHCF electrode and its rapid kinetics arising from pseudocapacitive effects (Fig. 2(b)). As the scan rate increased from 1 to 20 $mV \cdot s^{-1}$, the contributions from capacitive-controlled processes were determined as 80%, 83%, 88%, 89%, and 95%, respectively (Fig. 2(c)). These data demonstrate that the capacitive-controlled mechanism dominates Li^{+} ions storage at elevated scan rates, with diminished contributions from diffusion-controlled processes, which is highly advantageous for accelerating the kinetics of pseudocapacitive Li^{+} ions (de)intercalation. Furthermore, the increasing capacitive contribution ratio with scan rate strongly corroborates the capacitive-dominated charge storage mechanism in CuHCF electrode. To evaluate the long-term cycling stability of CuHCF electrode in 1.0 $mol \cdot L^{-1}$ LiCl solution, GCD tests were conducted at a current density of 1.0 $A \cdot g^{-1}$. As depicted in Fig. 2(d), the capacitance retention remained at approximately 99.4% after 1000 cycles, unequivocally demonstrating the exceptional electrochemical stability of CuHCF electrode under prolonged operational conditions.

3.3. Deionization capability test

To systematically evaluate the Li^{+} ions electrosorption performance, a HCDI unite was constructed employing CuHCF nanoparticles as the cathode and A-AC (synthesized following our previously reported methodology [34]) as the anode for comprehensive electrosorption characterization. The electrochemical performance of the AC electrode was evaluated in a 1 $mol \cdot L^{-1}$ LiCl aqueous solution. As depicted in Fig. S6(a), the CV curves recorded at scan rates ranging from 1 to 10 $mV \cdot s^{-1}$ exhibit a nearly rectangular shape, indicating ideal electric double-layer capacitive behavior with excellent electrochemical reversibility. GCD measurements were further conducted on the AC sample at current densities varying from 0.5 to 2.0 $A \cdot g^{-1}$. As shown in Fig. S6(b)–(c), the specific capacitance of AC was determined to be 117.7 $F \cdot g^{-1}$ at a current density of 0.25 $A \cdot g^{-1}$. Long-term cyclic tests were conducted in 500 $mg \cdot L^{-1}$ LiCl solution under precisely controlled operational parameters, with each complete charge—discharge cycle maintained at approximately 35 min (Figs. 3(a) and S7(a)). The dynamic conductivity monitoring revealed that the CuHCF

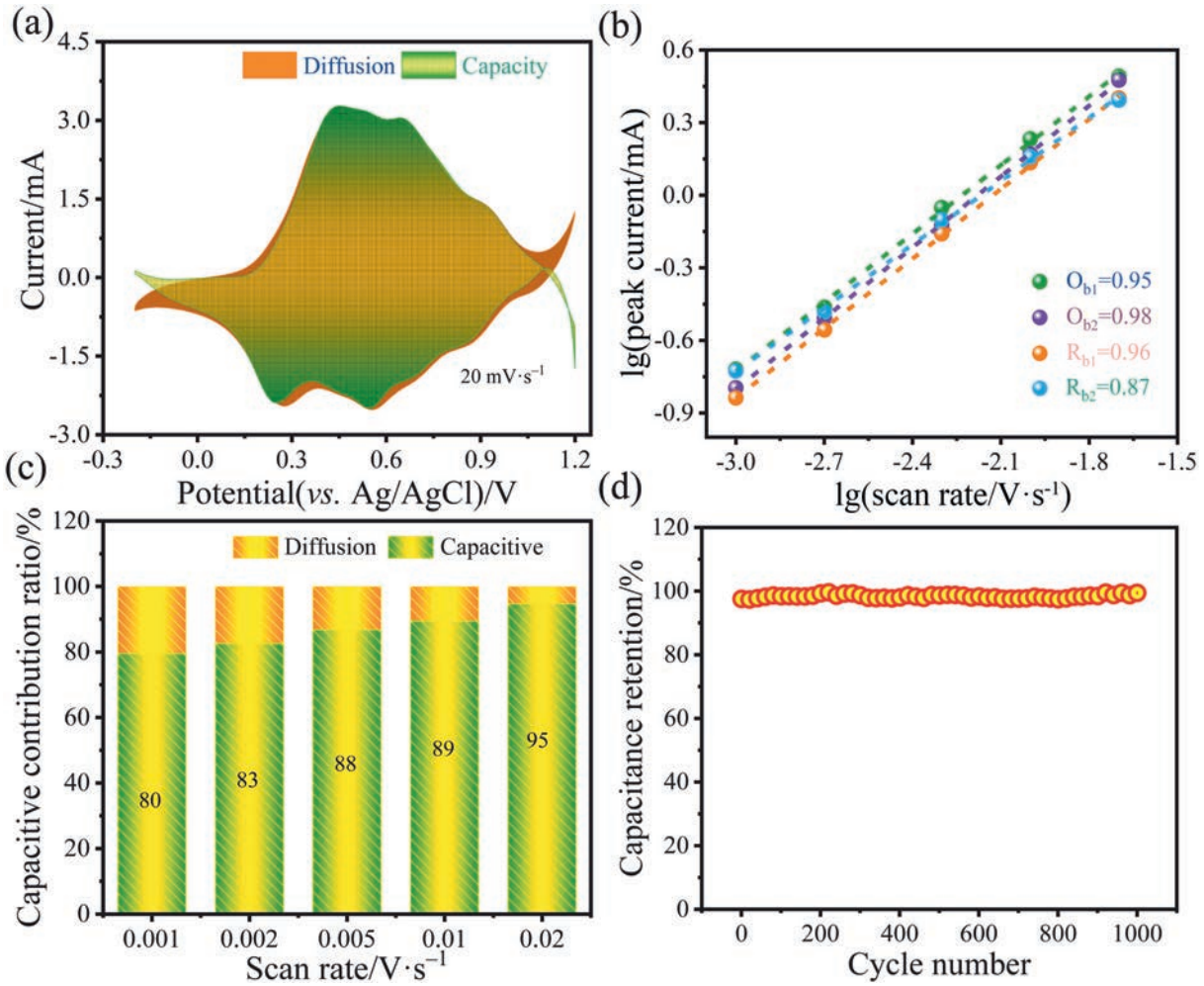

Fig. 2. (a) The capacitance behavior and diffusion behavior of CuHCF electrode at 20 mV·s^{-1}. (b) lg(peak current, mA) and lg(sweep speed, mV·s^{-1}) curves of CuHCF electrode based on CV. (c) The capacitance-controlled and diffusion-controlled contribution of CuHCF electrode at various scan rates. (d) Long-time cyclic performance of CuHCF electrode at current density of 1 A·g^{-1}.

electrode demonstrated reversible capture and release of Li^+ ions during the insertion and extraction processes, achieving remarkable electrosorption capacities ranging from 24.5 to 25.5 mg·g^{-1}. Furthermore, the current response profiles exhibited exceptional stability throughout consecutive cycling operations, thereby substantiating the superior electrochemical reversibility and outstanding cycling durability of the CuHCF electrode architecture towards Li^+ ions (de)intercalation mechanisms. This robust performance underscores the structural integrity and electrochemical stability of the CuHCF framework in HCDI application.

To further investigate the electrosorption performance and kinetic behavior of Li^+ ions on the CuHCF electrode, systematic evaluations were conducted under varying applied voltages (0.6–1.4 V) and LiCl solution concentrations (300–1000 mg·L^{-1}). As presented in Fig. 3(b), the applied voltage had a significant influence on the Li^+ ions electrosorption characteristics, with progressively enhanced conductivity variations observed upon increasing the voltage from 0.6 V to 1.4 V, reaching maximum conductivity reduction at 1.4 V. Corresponding current response profiles (Fig. S7(b)) revealed a positive correlation between applied voltage and current intensity, demonstrating voltage-dependent electrochemical activation. Fig. 3(c) delineated Li^+ ions electrosorption capacities of 11.0, 15.0, 20.5, 25.5, and 26.5 mg·g^{-1} with associated CE of 59%, 60%, 62%, 94%, and 47% at 0.6, 0.8, 1.0, 1.2, and 1.4 V, respectively, indicating enhanced Li^+ capture capability at elevated voltages. Notably, when the applied voltage exceeded 1.2 V, a marked decline in CE was observed, which could be attributed to parasitic reactions (*e.g.*, water electrolysis) occurring at the electrode–electrolyte interface.

As illustrated in Fig. 3(d), the electroadsorption capacity of the CuHCF electrode steadily increases with the concentration of Li^+ ions. Specifically, at an initial LiCl concentration of 300 mg·L^{-1}, the electroadsorption capacity reaches 19.0 mg·g^{-1}. When the LiCl concentration is increased to 500, 700, 1000, and 2000 mg·L^{-1}, the electroadsorption capacities correspondingly attain values of 25.5, 27.0, 30.5, and 40.0 mg·g^{-1}. This observation suggests that elevating the concentration of LiCl solution enhances the conductivity of the feed solution, thereby reducing the overall resistance of the HCDI module. This reduction in resistance facilitates the migration of salt ions from the feed solution channel into the electrode pores, ultimately improving the Li^+ ions extraction performance.

To elucidate the rate-controlling mechanism of Li^+ ions (de) intercalation behavior on CuHCF electrodes, a comprehensive kinetic analysis was systematically conducted to investigate the interfacial processes. The electrosorption kinetics under an applied potential of 1.2 V were initially examined through pseudo-first-order and pseudo-second-order kinetic models (Fig. S8(a)) [35,36]. The pseudo-first-order model, typically describing physical adsorption mechanisms, yielded a determination coefficient

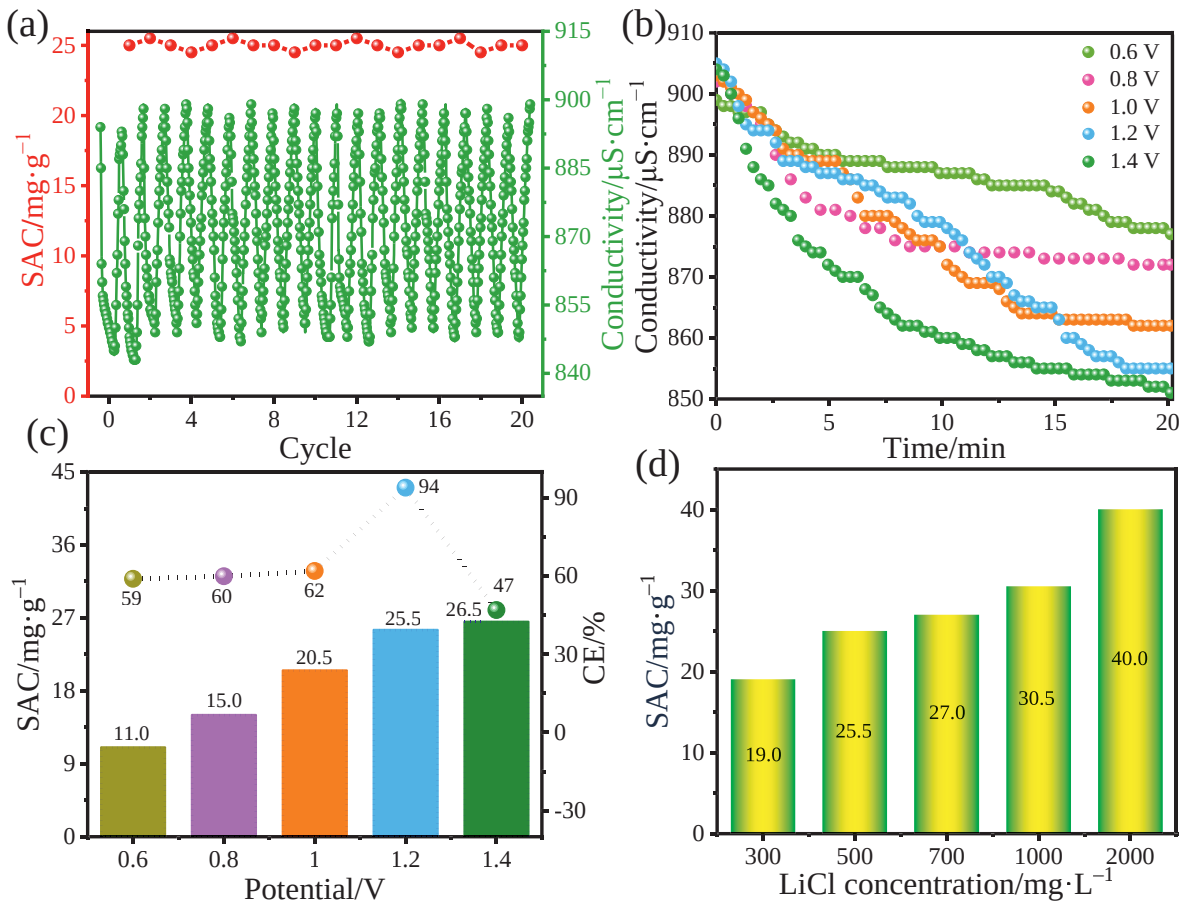

Fig. 3. (a) HCDI cycling abilities of CuHCF electrode in 500 mg·L^{-1} LiCl solution at 1.2 V. (b) Electroadsorption curves of CuHCF electrode at 0.6–1.4 V. (c) Electroadsorption capacity and charge efficiency of CuHCF electrode at 0.6–1.4 V. (d) Electroadsorption capacity of CuHCF electrode at 300–2000 mg·L^{-1} LiCl solution.

(R^2) of 0.988, while the pseudo-second-order model, which accounts for both physical and chemisorption interactions, demonstrated superior fitting performance with an R^2 value of 0.992 (Table S1). This comparative analysis strongly suggests a hybrid adsorption mechanism involving charge-transfer processes and surface complexation. Further investigations revealed a concentration-dependent enhancement in Li^+ ions electrosorption capacity, attributed to the intensified electric field driving force derived from elevated ionic concentrations (Fig. S8(b)). The observed linear correlation between initial Li^+ ions concentration and equilibrium adsorption capacity was quantitatively analyzed using the Langmuir isotherm model, which exhibited remarkable consistency with experimental data ($R^2 = 0.968$). This high-degree correspondence not only validates the model's applicability but also provides compelling evidence for the homogeneous distribution of active adsorption sites across the CuHCF electrode surface.

3.4. Selective electrosorption Li^+ ions

In natural salt lake brines, the chemical properties of Li^+ and Mg^{2+} are similar, posing challenges in the extraction of lithium through conventional methods such as evaporation, physical adsorption, and solvent extraction. The co-extraction of Mg^{2+} alongside Li^+ necessitates additional post-treatment steps, thereby escalating both the cost and time required. Consequently, the selective separation of Mg^{2+} and Li^+ ions emerges as a critical aspect of Li^+ ions extraction. To investigate the selective electrosorption capability of CuHCF electrodes in the HCDI process for Li^+ ions, experiments were conducted using solutions of 500 mg·L^{-1} LiCl and $MgCl_2$ at an operating voltage of 1.2 V. The analysis compared the electrosorption behavior of CuHCF electrodes for both Li^+ and Mg^{2+} ions (Fig. S9(a)). The saturation adsorbed amount of Li^+ ions on the CuHCF electrode was determined to be 25.5 mg·g^{-1}, which is 2.55 times greater than that for Mg^{2+} ions at 10 mg·g^{-1}. Fig. S9(b) illustrates the energy efficiency of electrosorption of Li^+ and Mg^{2+} ions on the CuHCF electrode. It is evident that the Ragone plot for Li^+ ions occupies the upper right region, indicating that the CuHCF exhibits a higher electrosorption capacity and faster extraction rate for Li^+ ions. Based on above results, the CE of the CuHCF electrode in LiCl and $MgCl_2$ solutions was calculated, revealing a superior CE for the electrosorption of Li^+ ions compared to Mg^{2+} ions (Fig. S9(c)).

Additionally, a mixed solution environment of Li^+ and Mg^{2+} ions was constructed to thoroughly analyze the selective electrosorption behavior of the CuHCF electrode. Various molar ratios of $MgCl_2$ to LiCl (5:1, 10:1, 15:1, and 30:1, with a fixed LiCl concentration of 3.3 mmol·L^{-1}) were employed to quantify the CuHCF electrode's selective adsorption capabilities in a high-concentration Mg^{2+} ions environment. Fig. S9(d) showcases the selective separation coefficient for Li^+ ions in mixed solutions at different molar ratios of LiCl and $MgCl_2$. In high Mg^{2+} ions solutions, the selectivity coefficient $\alpha_{Li/Mg}$ reached 3.1. This high selectivity for Li^+ ions is primarily attributed to the cubic crystal structure characteristics of CuHCF electrode, wherein the significant hydration of Mg^{2+} hinders its incorporation into the CuHCF

lattice. The results indicate that even in the presence of high Mg^{2+} ions concentrations, CuHCF electrode maintains a pronounced selective electrosorption capability for Li^+ ions. However, lithium-containing brines are often complicated by the presence of various monovalent competing ions, such as Na^+ and K^+. Therefore, in this work, an HCDI system employing a CuHCF electrode was utilized to evaluate the electrosorption behavior in the presence of these competing ions at mass concentrations equal to that of Li^+. As illustrated in Fig. S10, the CuHCF electrode exhibited a significantly higher electrosorption capacity for Li^+ ions compared to both Na^+ and K^+ ions, further demonstrating its strong potential for application in lithium extraction from brine resources.

3.5. Selective electrosorption Li^+ ions mechanism

To further investigate the selective electroadsorption behavior of the CuHCF electrode, the electrochemical characteristics of the CuHCF electrode were studied in different electrolytes (1.0 $mol \cdot L^{-1}$ LiCl and $MgCl_2$). Fig. S11(a) displays the CV curves of the CuHCF electrode recorded in LiCl and $MgCl_2$ electrolytes at a scan rate of 1 $mV \cdot s^{-1}$. In the LiCl electrolyte, two pairs of redox peaks are distinctly observed, which are associated with the redox processes of Cu and Fe within the CuHCF framework, accompanied by the insertion and extraction of Li^+ ions. In contrast, in the $MgCl_2$ electrolyte, only a single pair of redox peaks can be identified (located at 0.28 V and 0.42 V), confirming the significant selectivity of the CuHCF electrode toward Li^+ ions throughout the electroadsorption process. Furthermore, the integrated area beneath the CV curve for the CuHCF electrode in the LiCl electrolyte is markedly larger than that observed in the $MgCl_2$ electrolyte, indicating a higher specific capacitance of the CuHCF electrode in LiCl solution. Additionally, the specific capacitance values of the CuHCF electrode in both LiCl and $MgCl_2$ solutions were calculated based on the obtained GCD curves. As shown in Fig. S11(b), the specific capacitance of the CuHCF electrode in LiCl solution surpasses that in $MgCl_2$ solution at various current densities. Notably, at a current density of 1 $A \cdot g^{-1}$, the specific capacitance in LiCl electrolyte (120.1 $F \cdot g^{-1}$) is significantly higher than that in $MgCl_2$ electrolyte (51.4 $F \cdot g^{-1}$), demonstrating the excellent lithium storage capability of the CuHCF electrode. This pronounced selectivity toward Li^+ ions is primarily attributed to the smaller hydrated ion radius and lower hydration energy of Li^+ ions, which facilitates their migration into the cubic architecture of CuHCF electrode. Conversely, the higher hydration energy of Mg^{2+} ions inhibits their entry into the active sites of CuHCF electrode. These findings indicate that the CuHCF electrode exhibits exceptional (de)intercalation capability and remarkable selectivity for Li^+ ions.

To elucidate the (de)intercalation mechanism of Li^+ ions during the HCDI process, non-*in situ* XRD and XPS analyses were conducted on the CuHCF electrode before and after the HCDI experiments. The XRD results indicate that no new diffraction peaks were observed, demonstrating the excellent structural stability of the CuHCF electrode throughout the HCDI process. However, after the electroadsorption of Li^+ ions, the XRD peaks shifted to higher angles compared to those of the initial CuHCF electrode, confirming the incorporation of Li^+ ions into the CuHCF framework (Fig. S11(c)). As illustrated in Fig. 4(a), the XPS spectra of the CuHCF electrode before and after Li^+ electrosorption demonstrate distinct

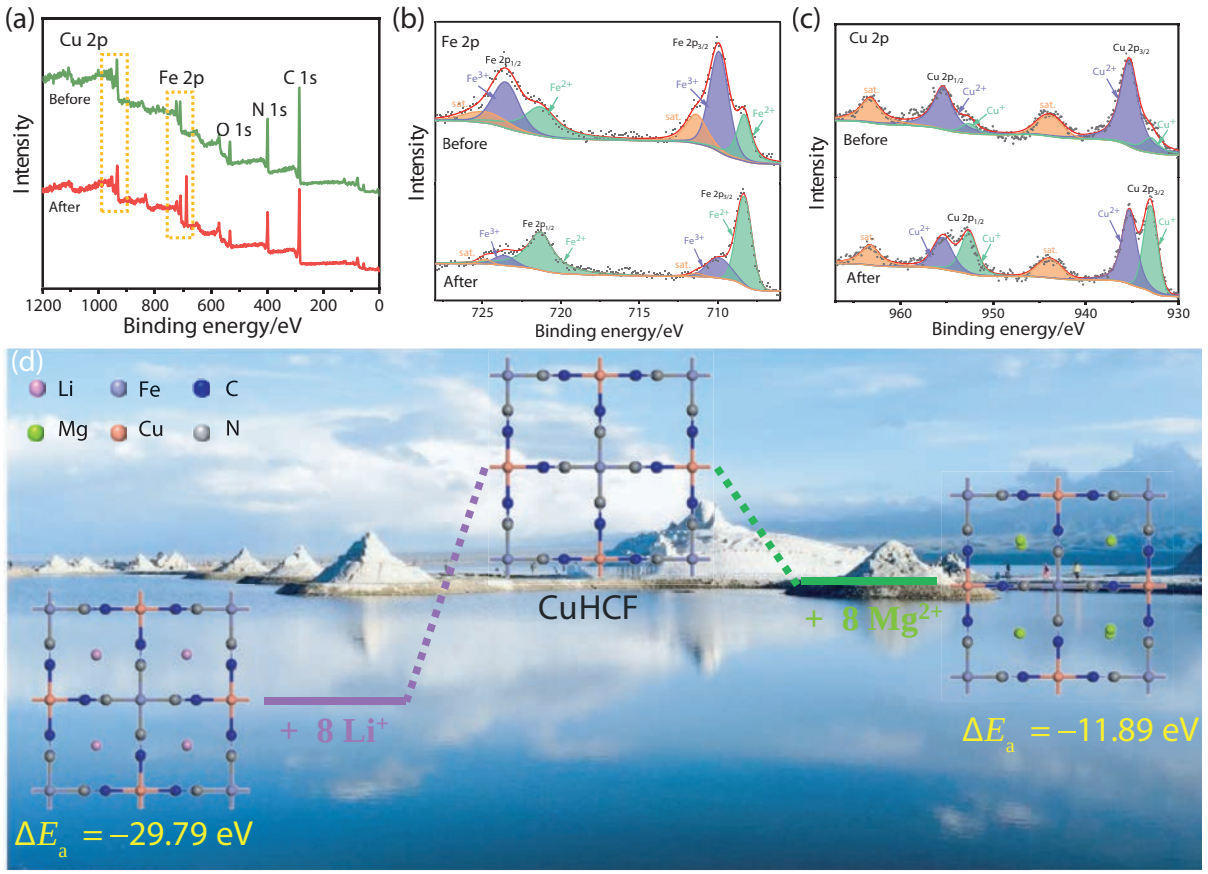

Fig. 4. (a) XPS survey spectrum, (b) Fe 2p and (c) Cu 2p XPS spectra of CuHCF electrode before and after electroadsorption of Li^+ ions. (d) Absorption models of the CuHCF electrode toward Li and Mg and absorption energies (ΔE_a).

binding energy shifts in Fe 2p and Cu 2p core levels toward lower energy regions, while other elemental peaks remain virtually unaltered. This observation confirms the occurrence of strong electronic interactions between the CuHCF framework and intercalated Li^+ ions. Fig. 4(b) further reveals that the post-electrosorption high-resolution Fe 2p spectrum retains characteristic features of the pristine CuHCF electrode. Nevertheless, a marked intensity enhancement is observed for peaks corresponding to Fe^{II} 2p orbitals, concomitant with a pronounced attenuation of Fe^{III} signatures (quantitative analysis indicates an increase in Fe^{II} content from 30.0% to 80.2%, while Fe^{III} content decreases from 70.0% to 19.8%). These redox-driven compositional changes unambiguously suggest the partial reduction of Fe^{3+} to Fe^{2+} during Li^+ ions insertion, thereby verifying the active participation of the $[Fe^{III}(CN)_6]^{4-}/[Fe^{II}(CN)_6]^{3-}$ redox couple in the lithium intercalation mechanism. As depicted in the high-resolution Cu 2p spectra (Fig. 4(c)), the post-electrosorption profile retains the characteristic peaks of Cu^{2+} at binding energies of 935.3 eV and 955.5 eV, exhibiting significant intensity attenuation. This is concomitant with a pronounced enhancement of Cu^+-associated peaks, as evidenced by quantitative deconvolution revealing an increase in Cu^+ content from 14.9% to 50.1%, alongside a decrease in Cu^{2+} content from 85.1% to 49.9%. This valence transition from Cu^{2+} to Cu^+ strongly correlates with Li^+ ions intercalation into the interstitial sites of the crystalline framework, suggesting that copper redox activity governs structural accommodation of Li^+ during the electrosorption process. The aforementioned results confirm that CuHCF electrode possesses a high selectivity for Li^+ ions extraction, facilitated by the dual redox dynamics of the $[Fe^{III}(CN)_6]^{4-}/[Fe^{II}(CN)_6]^{3-}$ and Cu^{2+}/Cu^+ couples, which cooperatively drive Li^+ ions insertion into lattice vacancies through charge compensation. The overall redox mechanism during electrosorption can be rationalized by a two-step process:

$$Cu_3^{II}\left[Fe^{III}(CN)_6\right]_2 + 3Li^+ + 3e^- \rightleftharpoons Li_3Cu_3^{I}\left[Fe^{III}(CN)_6\right]_2 \quad (5)$$

$$Cu_3^{II}\left[Fe^{III}(CN)_6\right]_2 + 2Li^+ + 2e^- \rightleftharpoons Li_2Cu_3^{II}\left[Fe^{II}(CN)_6\right]_2 \quad (6)$$

To further unearth the extraction ability of Li/Mg on the CuHCF electrode, the first-principles method based on the DFT are applied to evaluate the uptake capability of Li/Mg [37–40]. Considering its geometric characteristic, 8 Li^+ or Mg^{2+} ions are simultaneously inserted into the interstitial sites, their average adsorption energies are −3.72 eV for Li^+ ions and −1.49 eV for Mg^{2+} ions in Fig. 4 (d), respectively, indicating preferred extraction ability of Li^+ ions compared to Mg^{2+} ions.

4. Conclusions

In summary, the CuHCF nanoparticles, synthesized *via* a simple co-precipitation method, exhibit a well-defined three-dimensional open framework structure. Using CuHCF as a pseudocapacitive cathode, a HCDI system was assembled with A-AC as the anode, successfully achieving high selectivity capacitive adsorption for Li^+ ions in a mixed cation solution (Li^+ and Mg^{2+}). Non-*in situ* XRD and XPS results reveal that the (de)intercalation of Li^+ ions during the HCDI process are closely associated with the redox pairs within the CuHCF lattice, specifically $[Fe^{III}(CN)_6]^{4-}/[Fe^{II}(CN)_6]^{3-}$ and Cu^{2+}/Cu^+. Moreover, in a binary mixed solution with a Mg^{2+} and Li^+ ions molar ratio of 30:1, an impressive selectivity separation coefficient of 3.1 was achieved, indicating the CuHCF electrode with high electrosorption selectivity towards Li^+ ions. This capacitive design relies on the intrinsic ion sieving properties of the pseudocapacitive electrode, facilitating the high selectivity of electrosorptive of Li^+ during the HCDI process. This research provides guidance for the development of specific ion-selective pseudocapacitive electrodes tailored for electrosorption applications.

CRediT Authorship Contribution Statement

Li Zhang: Methodology, Investigation, Data curation. Shuyu Wang: Methodology, Investigation, Data curation. Cuijiao Zhao: Writing – review & editing, Validation, Project administration, Funding acquisition, Conceptualization. Menglong Liu: Methodology, Investigation, Data curation. Tao Ye: Methodology, Data curation. Wenwen Ding: Writing – review & editing. Hongjian Zhou: Writing – review & editing. Zhongti Sun: Writing – review & editing. Weiji Dai: Writing – review & editing. Saifang Huang: Writing – review & editing, Supervision.

Declaration of Competing Interest

The authors declare that they have no known competing financial interests or personal relationships that could have appeared to influence the work reported in this paper.

Acknowledgements

This research is supported by the National Natural Science Foundation of China (52202093), Postgraduate research & practice innovation program of Jiangsu province (SJCX25_2553), the China Postdoctoral Science Foundation (2023M731357), and the open project of Anhui Province Key Laboratory of Efficient Conversion and Solid-State Storage of Hydrogen & Electricity (ECS-SHE2024KF03). We thank the theoretical calculations performed on the Northwest District of the Sugon National Supercomputer Center and the A6 Zone of the Beijing Super Cloud Computing Center, supported by PARATERA.

Supplementary Material

Supplementary data to this article can be found online at https://doi.org/10.1016/j.cjche.2025.09.008.

References

[1] X. Sun, M.G. Ouyang, H. Hao, Surging lithium price will not impede the electric vehicle boom, *Joule* 6 (8) (2022) 1738–1742.
[2] X.Y. Zhao, S. Yang, Y.D. Hou, H.Q. Gao, Y.F. Wang, D.A. Gribble, V.G. Pol, Recent progress on key materials and technical approaches for electrochemical lithium extraction processes, *Desalination* 546 (2023) 116189.
[3] X.Y. Zhao, H.C. Yang, Y.F. Wang, Z.L. Sha, Review on the electrochemical extraction of lithium from seawater/brine, *J. Electroanal. Chem.* 850 (2019) 113389.
[4] A. Khalil, S. Mohammed, R. Hashaikeh, N. Hilal, Lithium recovery from brine: recent developments and challenges, *Desalination* 528 (2022) 115611.
[5] Y. Zhang, W. Sun, R. Xu, L. Wang, H.H. Tang, Lithium extraction from water lithium resources through green electrochemical-battery approaches: a comprehensive review, *J. Clean. Prod.* 285 (2021) 124905.
[6] Y. Sun, Y.H. Wang, Y. Liu, X. Xiang, Highly efficient lithium extraction from brine with a high sodium content by adsorption-coupled electrochemical technology, *ACS Sustainable Chem. Eng.* 9 (33) (2021) 11022–11031.
[7] R. Zhu, S.X. Wang, C. Srinivasakannan, S.W. Li, S.H. Yin, L.B. Zhang, X.B. Jiang, G.L. Zhou, N. Zhang, Lithium extraction from salt lake brines with high magnesium/lithium ratio: a review, *Environ. Chem. Lett.* 21 (3) (2023) 1611–1626.
[8] G. Liu, Z.W. Zhao, A. Ghahreman, Novel approaches for lithium extraction from salt-lake brines: a review, *Hydrometallurgy* 187 (2019) 81–100.
[9] Y. Sun, Q. Wang, Y.H. Wang, R.P. Yun, X. Xiang, Recent advances in magnesium/lithium separation and lithium extraction technologies from salt lake brine, *Sep. Purif. Technol.* 256 (2021) 117807.

[10] X.D. Zhang, K.C. Zuo, X.R. Zhang, C.Y. Zhang, P. Liang, Selective ion separation by capacitive deionization (CDI) based technologies: a state-of-the-art review, *Environ. Sci.: Water Res. Technol.* 6 (2) (2020) 243–257.
[11] L. Chang, Y.H. Fei, Y.H. Hu, Structurally and chemically engineered graphene for capacitive deionization, *J. Mater. Chem. A* 9 (3) (2021) 1429–1455.
[12] B. Hu, X.H. Shang, P.F. Nie, B.S. Zhang, J.M. Yang, J.Y. Liu, Lithium ion sieve modified three-dimensional graphene electrode for selective extraction of lithium by capacitive deionization, *J. Colloid Interface Sci.* 612 (2022) 392–400.
[13] G.Q. Ma, Y.S. Xu, A.J. Cai, H.J. Mao, X.Y. Zhang, D.M. Shin, L. Wang, H.J. Zhou, Binder-free $LiMn_2O_4$ nanosheets on carbon cloth for selective lithium extraction from brine *via* capacitive deionization, *Small* 20 (9) (2024) e2306530.
[14] J.G. Zhou, S.H. Xiang, X.Y. Wang, D.M. Shin, H.J. Zhou, Highly selective lithium extraction from salt lake *via* carbon-coated lithium vanadium phosphate capacitive electrode, *Chem. Eng. J.* 482 (2024) 148985.
[15] J.G. Zhou, Y.S. Xu, D.M. Shin, H.J. Zhou, Breaking the trade-off between capacity, stability, and selectivity for electrochemical lithium extraction *via* a dual-ion doping strategy, *Desalination* 600 (2025) 118530.
[16] G. Liao, L.L. Yu, Y.F. Xia, Z.M. Wang, Z.J. Lu, J.C. Mei, H.L. Liu, C.B. Liu, High selectivity, capacity and stability for electrochemical lithium extraction on boron-doped $H_{1.6}Mn_{1.6}O_4$ by tailoring lattice constant and intercalation energy, *Water Res.* 274 (2025) 123131.
[17] K. Wang, Y. Liu, Z.B. Ding, Y.Q. Li, T. Lu, L.K. Pan, Metal–organic-frameworks-derived $NaTi_2(PO_4)_3$/carbon composites for efficient hybrid capacitive deionization, *J. Mater. Chem. A* 7 (19) (2019) 12126–12133.
[18] Y.Q. Li, Z.B. Ding, X.L. Zhang, J.L. Li, X.J. Liu, T. Lu, Y.F. Yao, L.K. Pan, Novel hybrid capacitive deionization constructed by a redox-active covalent organic framework and its derived porous carbon for highly efficient desalination, *J. Mater. Chem. A* 7 (44) (2019) 25305–25313.
[19] Y.Q. Li, Z.B. Ding, J.F. Li, J.B. Li, T. Lu, L.K. Pan, Highly efficient and stable desalination *via* novel hybrid capacitive deionization with redox-active polyimide cathode, *Desalination* 469 (2019) 114098.
[20] Y.S. Xu, H.J. Zhou, G.Z. Wang, Y.X. Zhang, H.M. Zhang, H.J. Zhao, Selective pseudocapacitive deionization of calcium ions in copper hexacyanoferrate, *ACS Appl. Mater. Interfaces* 12 (37) (2020) 41437–41445.
[21] Q. Liu, C.Y. Zhao, M.H. Yuan, L.P. Liu, X.H. Liu, Y.J. Liu, Z.Q. Liu, L. Tong, A.G. Ying, A dynamic intercalation mechanism in pre-intercalation carbon nanosheets for capacitive deionization cells, *Desalination* 535 (2022) 115842.
[22] C.Y. Zhang, D. He, J.X. Ma, W.W. Tang, T.D. Waite, Faradaic reactions in capacitive deionization (CDI) - problems and possibilities: a review, *Water Res.* 128 (2018) 314–330.
[23] S. Bae, S.I. Jeon, W. Lee, Y. Kim, K. Cho, Four-step constant voltage operation of hybrid capacitive deionization with composite electrodes for bifunctional deionization and lithium recovery, *Desalination* 565 (2023) 116883.
[24] X.H. Shang, B. Hu, P.F. Nie, W. Shi, T. Hussain, J.Y. Liu, $LiNi_{0.5}Mn_{1.5}O_4$-based hybrid capacitive deionization for highly selective adsorption of lithium from brine, *Sep. Purif. Technol.* 258 (2021) 118009.
[25] Z.Z. Liu, W. Xi, H.B. Li, The feasibility of hollow echinus-like $NiCo_2O_4$ nanocrystals for hybrid capacitive deionization, *Environ. Sci.: Water Res. Technol.* 6 (2) (2020) 283–289.
[26] A. Siekierka, B. Tomaszewska, M. Bryjak, Lithium capturing from geothermal water by hybrid capacitive deionization, *Desalination* 436 (2018) 8–14.
[27] Y.X. Chen, Y.F. Yuan, C.L. Mo, P.F. Du, S.Y. Guo, Yolk-shell Co-glycerate@Fe–Co Prussian blue analogue spheres for high-performance lithium-ion batteries, *Mater. Lett.* 320 (2022) 132358.
[28] T. Yamashita, P. Hayes, Analysis of XPS spectra of Fe^{2+} and Fe^{3+} ions in oxide materials, *Appl. Surf. Sci.* 254 (8) (2008) 2441–2449.
[29] P. Jiang, H.Z. Shao, L. Chen, J.W. Feng, Z.P. Liu, Ion-selective copper hexacyanoferrate with an open-framework structure enables high-voltage aqueous mixed-ion batteries, *J. Mater. Chem. A* 5 (32) (2017) 16740–16747.
[30] M. Rethinasabapathy, G. Bhaskaran, S.K. Hwang, T. Ryu, Y.S. Huh, Efficient lithium extraction using redox-active Prussian blue nanoparticles-anchored activated carbon intercalation electrodes *via* membrane capacitive deionization, *Chemosphere* 336 (2023) 139256.
[31] J.L. Cao, Y. Wang, L. Wang, F. Yu, J. Ma, $Na_3V_2(PO_4)_3$@C as faradaic electrodes in capacitive deionization for high-performance desalination, *Nano Lett.* 19 (2) (2019) 823–828.
[32] V. Augustyn, P. Simon, B. Dunn, Pseudocapacitive oxide materials for high-rate electrochemical energy storage, *Energy Environ. Sci.* 7 (5) (2014) 1597–1614.
[33] V. Augustyn, J. Come, M.A. Lowe, J.W. Kim, P.L. Taberna, S.H. Tolbert, H.D. Abruña, P. Simon, B. Dunn, High-rate electrochemical energy storage through Li^+ intercalation pseudocapacitance, *Nat. Mater.* 12 (6) (2013) 518–522.
[34] C.J. Zhao, G.Q. Liu, N. Sun, X. Zhang, G.Z. Wang, Y.X. Zhang, H.M. Zhang, H.J. Zhao, Biomass-derived N-doped porous carbon as electrode materials for Zn–air battery powered capacitive deionization, *Chem. Eng. J.* 334 (2018) 1270–1280.
[35] B.H. Hameed, A.A. Ahmad, N. Aziz, Isotherms, kinetics and thermodynamics of acid dye adsorption on activated palm ash, *Chem. Eng. J.* 133 (1–3) (2007) 195–203.
[36] Y.S. Ho, G. McKay, Pseudo-second order model for sorption processes, *Process. Biochem.* 34 (5) (1999) 451–465.
[37] M. Dabbour, H. Jiang, B.K. Mintah, H. Wahia, R.H. He, Ultrasonic-assisted protein extraction from sunflower meal: kinetic modeling, functional, and structural traits, *Innov. Food Sci. Emerg. Technol.* 74 (2021) 102824.
[38] F.R. Hou, W.H. Ding, W.J. Qu, A.O. Oladejo, F. Xiong, W.W. Zhang, R.H. He, H.L. Ma, Alkali solution extraction of rice residue protein isolates: influence of alkali concentration on protein functional, structural properties and lysinoalanine formation, *Food Chem.* 218 (2017) 207–215.
[39] J.Y. Shi, Y.Y. Wang, Z.H. Li, X.W. Huang, T.T. Shen, X.B. Zou, Simultaneous and nondestructive diagnostics of nitrogen/magnesium/potassium-deficient cucumber leaf based on chlorophyll density distribution features, *Biosyst. Eng.* 212 (2021) 458–467.
[40] Z.P. Zhang, R.Y. Zhou, L.J. Ke, J.B. Li, H. Jayan, H.R. El-Seedi, X.B. Zou, Z.M. Guo, Development of multifunctional metal-organic frameworks (MOFs)-based nanofiller materials in food packaging: a comprehensive review, *Trends Food Sci. Technol.* 154 (2024) 104771.